ornl

ORNL/TM-10186

OAK RIDGE NATIONAL LABORATORY

MARTIN MARIETTA

Emittance of the ORNL Negative Ion Source

J. J. Donaghy
W. K. Dagenhart
K. L. Kannan
P. M. Ryan
W. L. Stirling
C. C. Tsai

OPERATED BY
MARTIN MARIETTA ENERGY SYSTEMS, INC.
FOR THE UNITED STATES
DEPARTMENT OF ENERGY

Printed in the United States of America. Available from
National Technical Information Service
U.S. Department of Commerce
5285 Port Royal Road, Springfield, Virginia 22161
NTIS price codes—Printed Copy: A03; Microfiche A01

ORNL/TM-10186
Dist. Category UC-20 a,d,f

Fusion Energy Division

EMITTANCE OF THE ORNL NEGATIVE ION SOURCE

J. J. Donaghy*
W. K. Dagenhart
K. L. Kannan
P. M. Ryan
W. L. Stirling
C. C. Tsai

DATE PUBLISHED — November 1987

*Washington and Lee University, Lexington, Virginia.

Funded by the
U.S. Department of Defense
under Interagency Agreement DOE No. 40-1442-84
and Army No. W31RPD-53-A180
with the
Office of Fusion Energy, U.S. Department of Energy

Prepared by the
OAK RIDGE NATIONAL LABORATORY
Oak Ridge, Tennessee 37831
operated by
MARTIN MARIETTA ENERGY SYSTEMS, INC.
for the
U.S. DEPARTMENT OF ENERGY
under Contract No. DE-AC05-84OR21400

CONTENTS

1. INTRODUCTION 1
2. DEFINITION AND MEASUREMENT OF EMITTANCE 2
3. ANALYSIS OF DATA 7
   3.1 CURRENT DENSITY MATRIX 8
   3.2 DETERMINING POINTS ON THE EMITTANCE DIAGRAM AND BEAM FRACTION 8
   3.3 RMS EMITTANCE 10
   3.4 BEAM PROFILE 10
   3.5 ANGULAR DISTRIBUTION 10
   3.6 ION TEMPERATURE 11
   3.7 TOTAL BEAM CURRENT 12
4. DISCUSSION OF RESULTS 13
5. DISCUSSION OF ERRORS 20
6. ACKNOWLEDGMENTS 23

ACKNOWLEDGMENTS 23

REFERENCES 24

ABSTRACT

An electrostatic emittance scanner has been used to measure the emittance of intense H^- and D^- beams formed by ion sources developed at the Oak Ridge National Laboratory (ORNL). The ion sources have been operated reliably in both the Surface Ionization with Transverse Extraction (SITEX) and Volume Ionization with Transverse Extraction (VITEX) modes. The emittance measurements were made in a magnetic field of about 1 kG. The effective dimensions of the beamlet sample at the accelerator exit in the SITEX mode were 0.21 cm by 0.16 cm. (Here 0.16 cm is the central part of a 12.7-cm beam ribbon that is parallel to the applied source magnetic field.) The normalized rms emittances for such SITEX beamlets ($\sim$1.14 mA) were 0.01 $\pi \cdot$ cm $\cdot$ mrad measured transverse to the field and 0.003 $\pi \cdot$ cm $\cdot$ mrad measured parallel to the field for 10-keV D^- beams (36 mA/cm^2). The dimensions of H^- beams at the accelerator exit in the VITEX mode were 0.1 cm by 2.0 cm. The normalized rms emittances were about 0.013 $\pi \cdot$cm $\cdot$mrad measured transverse to the field and 0.017 $\pi \cdot$ cm $\cdot$ mrad measured parallel to the field for 15-keV, 12-mA (or 60-mA/cm^2) beams. The highest current density achieved is above 150 mA/cm^2. Ion temperatures obtained from the parallel emittance measurements were 9.4 eV for SITEX beams and 0.6 eV for VITEX beams. In this report, the method used to analyze the measured emittance data is described, and the potential errors in measurement are discussed.

1. INTRODUCTION

Emittance measurements have been carried out for the ORNL negative ion sources. The emittance and ion temperature of these sources were previously estimated using a combination of beam profile measurements and calculations with the ORNL beam optics computer code.[1] The measurements discussed in this report were made with an electrostatic emittance scanner designed by the negative ion group at Los Alamos National Laboratory (LANL).[2] The scanner design required minor modifications for use in the ORNL source. Measurements have been made for both the SITEX (Surface Ionization with Transverse Extraction) and VITEX (Volume Ionization with Transverse Extraction) sources. Ion temperatures for the two sources have been determined by comparing scan data with a Maxwellian model.

A brief discussion of emittance and the method used to measure it is given in Sect. 2. Section 3 contains a discussion of the method used to analyze the data, Sect. 4 a discussion of the results, and Sect. 5 a brief discussion of the principal sources of error.

2. DEFINITION AND MEASUREMENT OF EMITTANCE

The orthogonal coordinates x, y, z are used to describe the geometry of the beam and the emittance scanner, where x is perpendicular to the magnetic field B, y is parallel to B, and z is the direction of beam propagation. Consider a beam moving along the z-axis. At each point along this axis, the beam may be characterized by a distribution function specifying the current density of the beam and its velocity distribution perpendicular to the z-axis. This distribution function depends on the coordinates x, y and the velocities $\dot{x}$ and $\dot{y}$. Emittance is usually measured[3,4] using the partial beam current density distribution $CD(x, x')$, where $x' = \dot{x}/\dot{z}$. Measurements must be made with two long slits in the y-direction so that the current density is effectively integrated over y and $\dot{y}$. An arrangement that may be used to measure $CD(x, x')$ is shown in Fig. 1. For each position x of the first slit, the second slit is moved over its entire range to record the angular (or velocity) distribution of the particles passing through the first slit. The first slit is then moved to a different position and the process repeated. In this way, the entire distribution can be mapped.

The partial distribution defines a surface in phase space with axes x, x', CD. A contour drawn on this surface at a fixed value of CD forms the boundary of the emittance diagram, and the area enclosed by the diagram is the emittance. If the maximum current density is denoted CD_{MAX} and the contour is drawn at a fraction

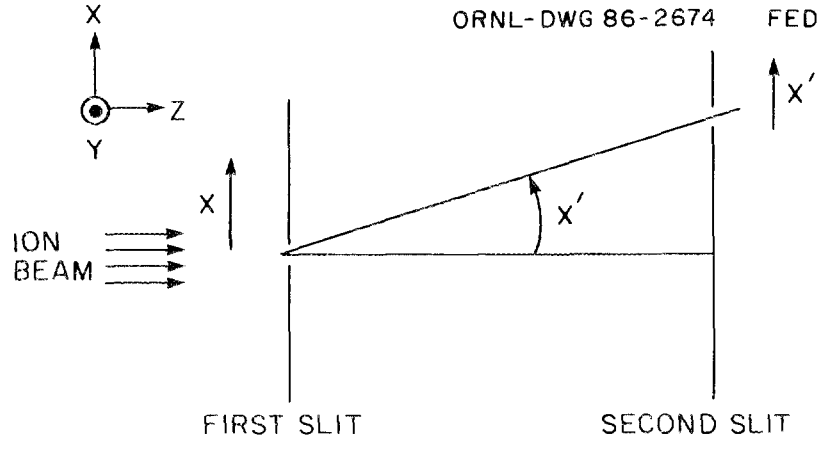

Fig. 1. Principle of the two-slit method.

t (called the threshold) of CD_{MAX}, the equation for the boundary of the emittance diagram is simply

$$CD(x,x') = t \cdot CD_{\mathrm{MAX}} .$$

The beam fraction for this threshold is the fraction of the total current enclosed by the emittance diagram at that threshold.

There are several variations of the two-slit method for measuring emittance. The emittance scanner used in the ORNL studies uses an electrostatic field to sweep the beam passing through the first slit across a fixed second slit.[2] The operation of the scanner is illustrated in Fig. 2. An ion with an energy $e\phi$ passing through the first slit at an angle $\theta \approx x'$ will be deflected through the second slit provided[2]

$$x' = \frac{V}{\phi}(D - 2\delta)/4g ,$$

where

V = potential difference between the deflection plates,
ϕ = potential difference through which the ions have been accelerated,
D = distance between the slits (which have a width s),
δ = distance between the deflection plates and the slits,
g = distance between the deflection plates.

The voltage V is scanned through a preselected range to obtain the angular distribution at a given position x. By repeating the measurements at different values of x, the partial distribution $CD(x,x')$ is obtained.

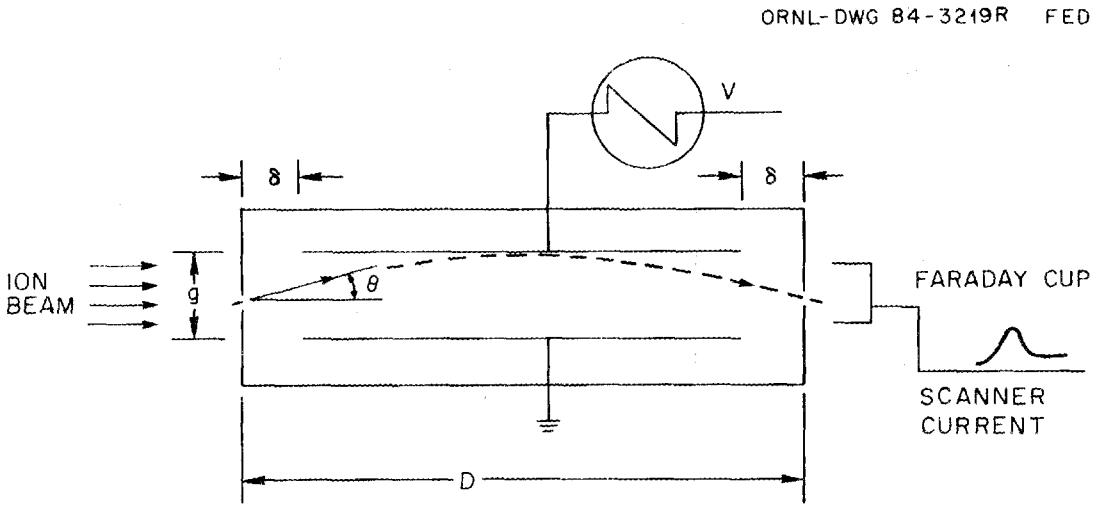

Fig. 2. Electrostatic emittance scanner.

The experimental arrangement used for the measurements is shown schematically in Fig. 3. The beam analyzed in the initial study is extracted through a long, narrow slit (12.7 by 0.21 cm) with the long dimension parallel to a fairly strong (about 1-kG) magnetic field and accelerated through a voltage of 10–20 kV. After traveling about 7.5 cm, the beam strikes a large Faraday cup that is used to measure the total beam current. This Faraday cup has a slit 0.16 by 2 cm with the long dimension perpendicular to the magnetic field. The effective beamlet dimensions for the SITEX source are thus 0.16 cm parallel to the field and 0.21 cm perpendicular to the field. For the VITEX source, the beam size is 0.1 by 2.0 cm at the accelerator exit. The large Faraday cup was withdrawn during the emittance measurements.

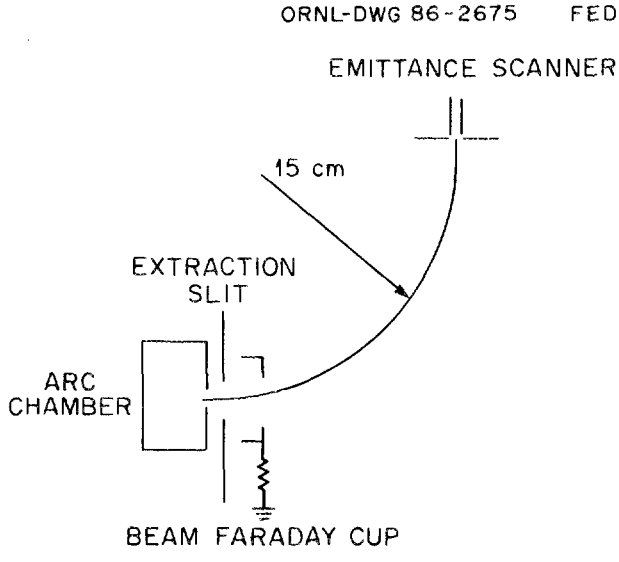

Fig. 3. Experimental arrangement for transverse emittance measurement; another emittance scanner (not shown) is used for parallel emittance measurement.

Drawings of the emittance scanner are shown in Fig. 4. Both scanner slits are 5 by 0.005 cm and are separated by $D = 4.128$ cm. The angular resolution is thus about 1.2 mrad. The deflection plates are separated by $g = 0.28$ cm, giving a maximum analyzable angle of ± 125 mrad. The deflection voltage is a ramp with a time duration of 25 ms. The digitized scanner currents are stored in standard CAMAC modules for subsequent analysis. Ten other fast channels were used to store digitized high voltage, beam current, etc. The data in these channels were used to reveal the beam condition and to monitor the performance of the source.

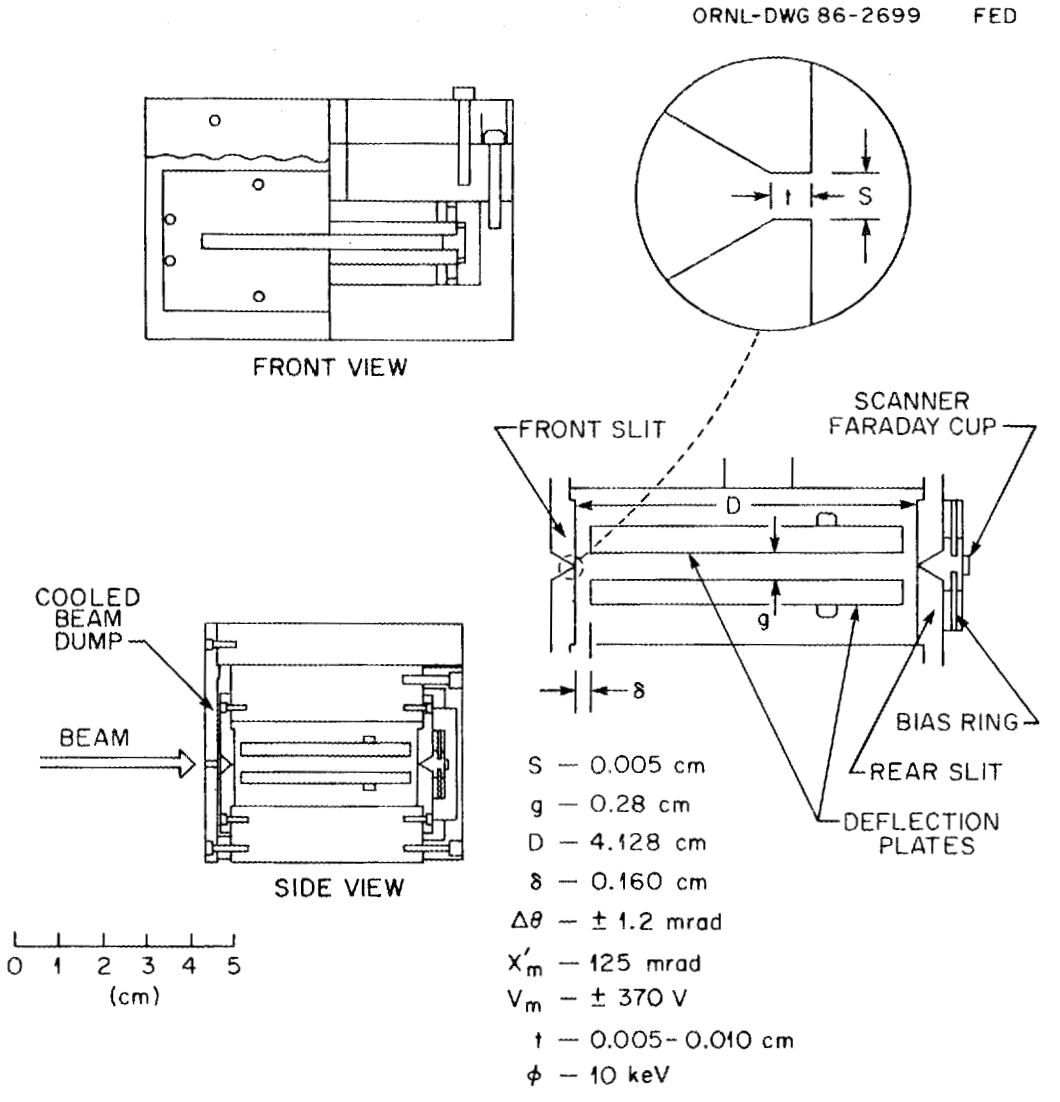

Fig. 4. Drawings of the emittance scanner.

The scanner was placed, by necessity, in the magnetic field. The beam ions travel from the slit to the scanner in a circle of radius 15 cm. The scanner is located at the 90° point on the circle. In passing through the scanner, the deflection from straight-line motion produced by the magnetic field is about 0.6 cm, if no compensating electrostatic field is used. For the measurements parallel to the field, this deflection causes no problem because the beam is narrow enough (~2 cm) and the scanner slits wide enough (5 cm) that the beam should pass through the scanner without loss. For the measurements transverse to the field, the magnetic deflection was cancelled for ions of mean velocity by applying a static electric field between the

deflection plates of the scanner. The beam spreads somewhat in passing through the scanner because of variations in the longitudinal velocity of the ions. This and other complications caused by the magnetic field are discussed in Sect. 5 of this report.

3. ANALYSIS OF DATA

The experimental current density distribution obtained in a typical measurement is shown in Fig. 5. These data were analyzed to obtain the following quantities:

1. coordinates of emittance diagrams for various thresholds,
2. normalized rms emittance vs beam fraction,
3. rms emittance,
4. beam (or current) profile,
5. angular distribution,
6. ion temperature, and
7. total current.

The code for the analysis uses no smoothing or curve-fitting procedures except in one of the ion temperature calculations. It has been tested using data generated

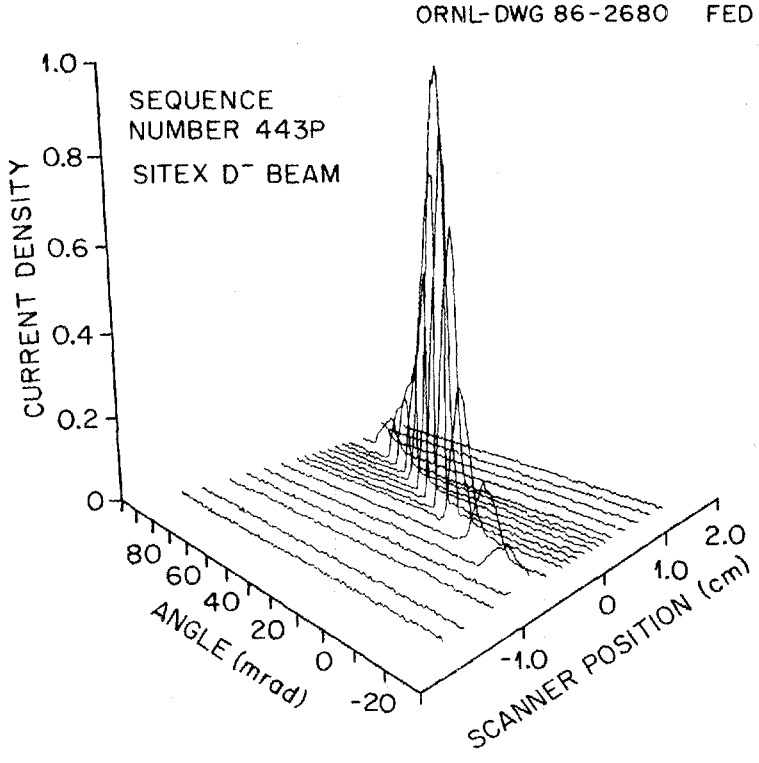

Fig. 5. Phase-space beam current density distribution for parallel emittance measurements of 1-keV, 9-mA D^- beams formed by the SITEX source.

from a Gaussian distribution (approximating the ORNL data) and data supplied by LANL. The values computed by the code agree very closely with those computed analytically from the Gaussian distribution, and the analysis of the LANL data also seems to agree well with their results.[5] The methods used in the code are described below.

3.1 CURRENT DENSITY MATRIX

The digitized current data from the scanner are stored in a two-dimensional array $CD(J, I)$, each column of which contains the digitized scanner currents at a given position $x(I)$ of the scanner. The scanner position is supplied as part of the raw data. The angle corresponding to the index J is computed as follows.

1. The step size of the angle is computed from the formula

$$\Delta\theta = (\Delta V/\phi)(D - 2\delta)/4g = 3.4\Delta V/\phi \ ,$$

where ΔV is the average difference in scanner voltage (in volts) between successive digitizer positions, ϕ is the accelerating voltage (in kilovolts), $D - 2\delta$ is the length of the scanner plates, and g is the gap distance between the deflection plates. The size of the angle step $\Delta\theta$ is thus computed in milliradians per division.

2. The angle θ is measured from the midpoint of the range of the angles scanned,

$$\theta(J) = (J - J_{\mathrm{MID}}) \cdot \Delta\theta \ ,$$

where J_{MID} is the number of digitizer divisions divided by 2. The peak scanner current at position $x(I)$ is denoted as $CD_{\mathrm{M}}(I)$, and the maximum scanner current in the whole measurement is CD_{MAX}.

3.2 DETERMINING POINTS ON THE EMITTANCE DIAGRAM AND BEAM FRACTION

The method used to determine points on the emittance diagram is illustrated in Fig. 6. The smooth curve represents the angular (or velocity) distribution at the position $x(I)$, and the "staircase" curve is the digitized scanner current. The code determines the angle location (index) of the largest current in each column $CD_{\mathrm{M}}(I)$. The angle index for column I is called $J_{\mathrm{M}}(I)$. If the largest current in column I is greater than the threshold current C_{MIN}, the code steps to the right and left to find the angles x_1' and x_2' at which the current drops below C_{MIN}.

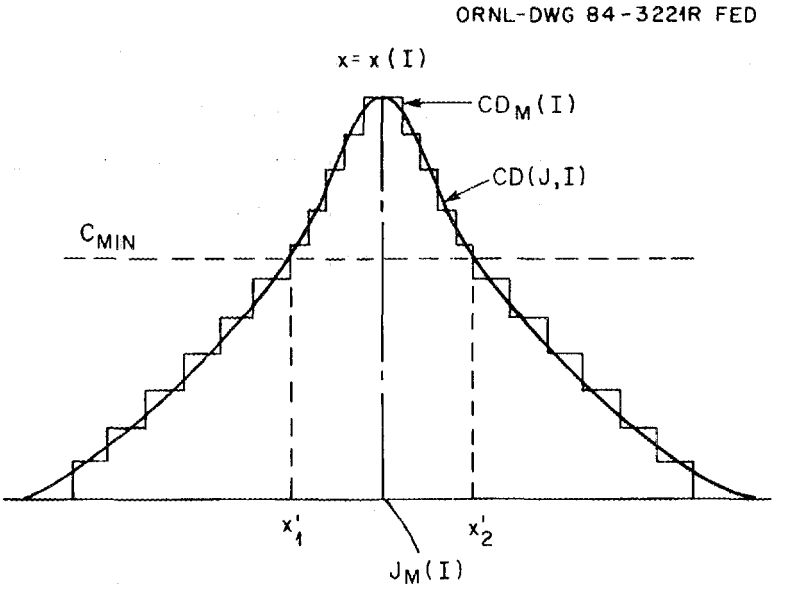

Fig. 6. Curves for angular current density distribution: smooth and staircase for SITEX parallel measurement.

Here the threshold current C_{MIN} equals the product of the threshold t and the maximum current CD_{MAX}. A linear interpolation is used to find precise values of these angles, though the angle steps are usually smaller than the angular resolution of the measurement. The angles thus located provide two points on the emittance diagram for a given threshold at each scanner position. The procedure is repeated at all positions $x(I)$ for which the maximum current is greater than C_{MIN}. If the maximum current for column I is less than C_{MIN}, the two angles are set equal to $[J_M(I) - J_{MID}]\Delta\theta$. (Points for which the angles are equal do not appear in the emittance plots. This is why the emittance diagram for a threshold of 0.9 sometimes turns out to be a straight line, since it has only two points. A minimum of four points is used in computing the area of an emittance plot.) Emittance diagrams are determined for thresholds ranging from 0.05 to 0.9 in steps of 0.05. The area $A(t)$ of each emittance diagram is computed by connecting the points with straight lines and computing the areas of the resulting trapezoids. The normalized emittance is computed from the equation

$$\epsilon(t) = (\beta\gamma/\pi)A(t) \quad (t = \text{threshold}) ,$$

where β is the ratio of the speed of the ions to the speed of light and $\gamma = (1-\beta^2)^{-1/2}$, which is very close to unity for the energies involved in the measurements.

Once the emittance diagram is determined, the beam fraction can be computed by integrating over that part of the distribution enclosed by the contour. The integration over the angle is carried out first using a simple trapezoidal routine. The area under the curve thus generated is computed by totaling the areas of rectangles centered on the points. This method of integration, though crude, introduces no significant error in this type of measurement.

3.3 RMS EMITTANCE

The normalized rms emittance is computed using the definition given by Allison,[6]

$$\epsilon(\text{rms}) = \beta\gamma\Big(\langle x^2\rangle\langle\theta^2\rangle - \langle x\theta\rangle^2\Big)^{1/2} .$$

The origin chosen for the calculation is the location of CD_{MAX}. The terms in this equation are computed from

$$\langle x^2\rangle = \sum_J \sum_I x^2(I)([CD(J,I) + CD(J+1,I)]/2)\Delta\theta\Delta x ,$$

and so on for $\langle\theta^2\rangle$ and $\langle x\theta\rangle^2$. The sum over θ is terminated when $CD(J,I) < 0.03\ CD_{\text{MAX}}$ to eliminate problems with background noise.

3.4 BEAM PROFILE

The beam (or current) profile is computed for each position $x(I)$ of the scanner from the equation

$$\text{CURPROF}(I) = \sum_J([CD(J,I) + CD(J+1,I)]/2)\Delta\theta .$$

The sum over J is again terminated when $CD(J,I) < 0.03\ CD_{\text{MAX}}$. The current profile can be used for estimating ion temperature at the source exit, if the ion temperature at the scanner is measured.

3.5 ANGULAR DISTRIBUTION

The angular distribution is computed from the equation

$$\text{ANGDIS}(J) = \sum_I CD(J,I)\Delta x(I) .$$

If $CD(J,I) < 0.03CD_{\mathrm{MAX}}$, CD is set equal to zero. If successive positions of the scanner are not closely spaced, the angular distribution computed from this equation may vary considerably from one angle to another simply because there will be gaps in the data at some angles. An alternative method that works better if scanner positions are widely spaced is to perform the integrations only at those angles $J_{\mathrm{M}}(I)$ corresponding to maxima in the scanner current. This method was used to compute the angular distribution curves shown in this report. The angular distribution is used to compute a value of ion temperature, as discussed in Sect. 3.6.

3.6 ION TEMPERATURE

The ion temperature at the source is computed from the measured scanner data in the direction parallel to the source magnetic field (because properties of beam ions are not affected by the applied magnetic field) in three ways, all of which assume a Maxwellian velocity distribution at the accelerator exit.[7] They are as follows:

First, the ion temperature is computed from the rms emittance using the equation

$$\epsilon(4\mathrm{rms}) = 4\epsilon(\mathrm{rms}) = \left[2SW(kT/Mc^2)^{1/2}\right]/3^{1/2} ,$$

where SW is the beam width at the accelerator exit. This equation is solved for kT,

$$kT = 12\epsilon^2(\mathrm{rms}) \cdot Mc^2/SW^2 .$$

The units used are such that kT is in electron volts.

Second, a least-squares fit is obtained for the emittance vs beam fraction curve. The equation for the beam fraction F corresponding to emittance ϵ is, for a Maxwellian distribution,

$$F = \mathrm{erf}\left[\pi\epsilon/\left(2SW(2kT/Mc^2)^{1/2}\right)\right] .$$

This can be solved for ϵ as

$$\epsilon = \left[\left(2SW(2kT/Mc^2)^{1/2}\right)/\pi\right]\mathrm{erf}^{-1}(F) = B\ \mathrm{erf}^{-1}(F) .$$

The coefficient B is determined by a least-squares method, from which kT can be computed. The values of the inverse error function are determined from a standard FORTRAN routine.

Third, the ion temperature is computed from the width at the $1/e$ points of the angular distribution,[8]

$$kT = e\phi\theta_w^2 \ ,$$

where θ_w is the half-width at the $1/e$ points. The $1/e$ points are determined by starting at the maximum of the angular distribution curve and stepping right and left until the current drops below $1/e$ times the maximum current. This method assumes that the angle enclosing a given fraction of the beam does not change as the beam moves from the accelerator exit to the scanner.

3.7 TOTAL BEAM CURRENT

The scanner current is converted to current density by dividing each value of $CD(J,I)$ by an element of phase-space area ΔA equal to the slit width times the angular resolution of the scanner. Then the total beam current is given by

$$\text{TOTAL} = \sum_{J,I} [CD(J,I)/\Delta A]\Delta\theta\Delta X \ .$$

It is assumed, of course, that the scanner samples the entire beam as it moves from its initial to its final position.

4. DISCUSSION OF RESULTS

For each emittance measurement, the phase-space beam current density distribution, as shown in Fig. 5, was measured, digitized, and stored by an emittance data acquisition system. The data were then analyzed as described in Sect. 3. Figures 7–10 show the results determined from measured parallel emittance data (Fig. 5) for a 1.14-mA beamlet in the central section of the 10-keV, 91-mA D^- beams formed in the SITEX mode. The beam profile of a 0.16-cm beamlet measured 24 cm downstream by the emittance scanner is shown in Fig. 7. The beam width between $1/e$ points of the curve in Fig. 7 is about 0.55 cm. The average ion temperature, determined from velocity scans of the beam ions, was 0.18 eV at the scanner. Assuming that the product of the ion temperature and the square of the beam width is conserved, we can estimate the ion temperature at the source to be 2.2 eV. Based on the angular distribution curve shown in Fig. 8, the ion temperature is about 2.7 eV. Figure 9 shows the phase-space emittance diagram; the corresponding rms emittance vs beam fraction curve is shown in Fig. 10. The normalized rms emittance is about 0.0029 $\pi \cdot \text{cm} \cdot \text{mrad}$. The corresponding ion temperature is about 8.3 eV. The smooth curve in this figure was obtained by fitting the emittance vs beam fraction

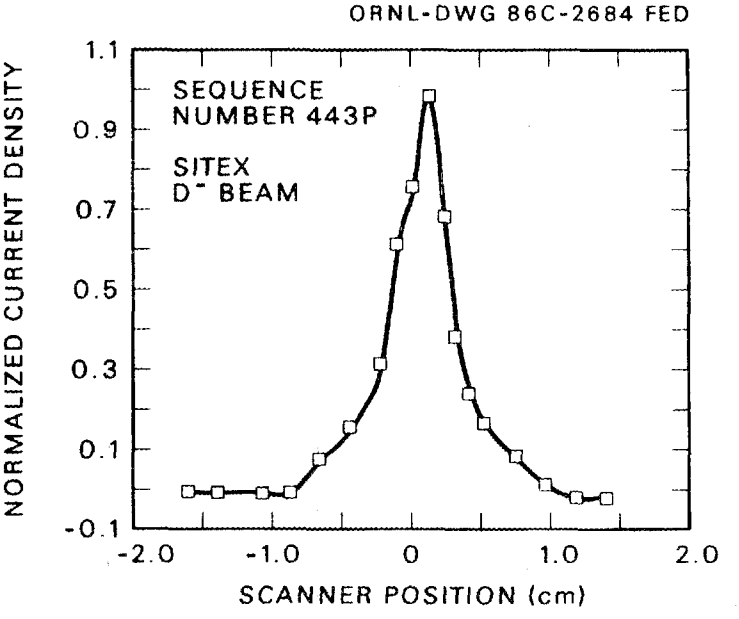

Fig. 7. Beam profile for scanner spatial position for SITEX parallel measurement.

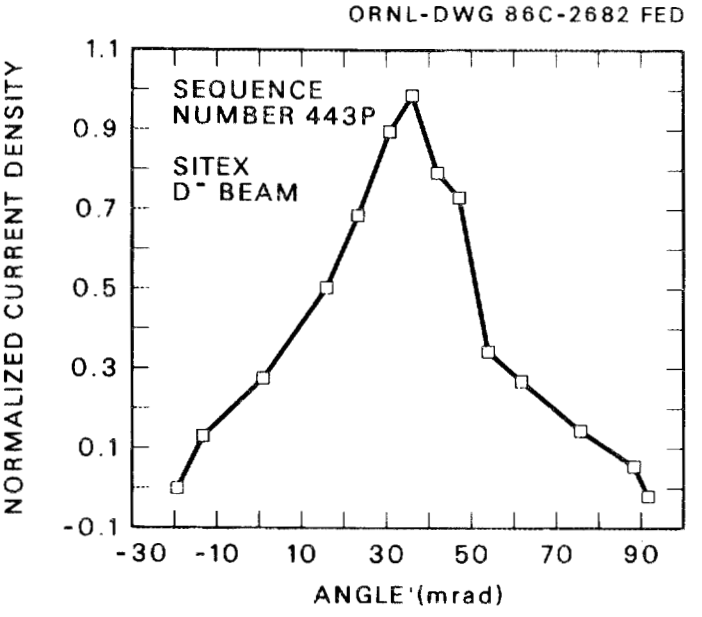

Fig. 8. Beam angular distribution for central fraction beams for SITEX parallel measurement.

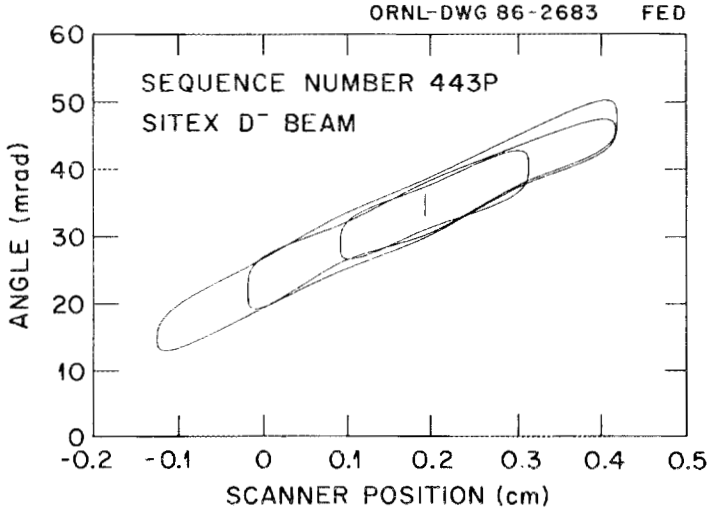

Fig. 9. Emittance program with curves for different threshold values for SITEX parallel measurement.

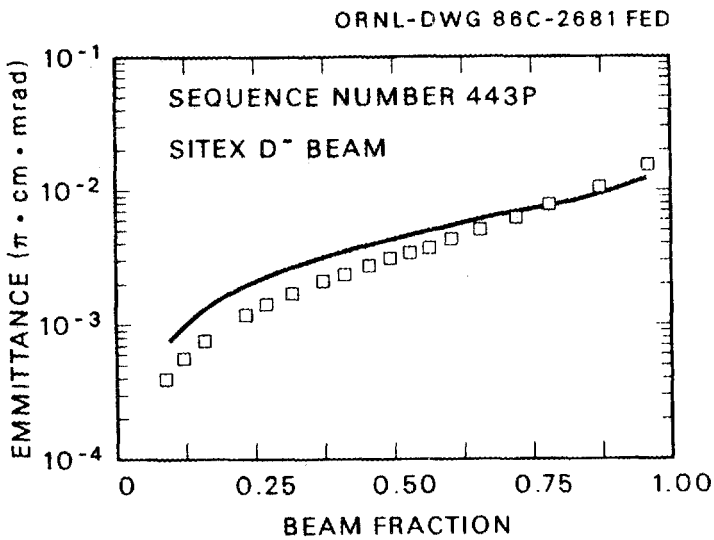

Fig. 10. RMS emittance vs beam fraction for SITEX parallel measurement.

curve to a Maxwellian distribution. The corresponding ion temperature is about 9.4 eV.

Comparing the ion temperatures calculated using these four methods, we find that the relatively low values from the first two methods are reasonable, because they are dominated by the ions in the beam center. For characterizing the entire beam, we should use the values determined from the last two methods. However, the ion temperature derived from the normalized rms emittance is by far the most erratic, because data noise of various types can shift the location of the maximum current far from the center of the distribution and thus produce anomalously large values of rms emittance. Usually the ion temperature deduced from the Gaussian fit of the emittance vs beam fraction curve is less erratic and thus is used to characterize the beam and is listed in Table 1.

Figures 11–15 show curves of the phase-space density distribution, the beam profile, the angular distribution, the emittance diagram, and the rms emittance vs beam fraction for the transverse emittance measurements of the 1.14-mA central beamlet for the 10-keV, 91-mA D^- beams formed by the SITEX source. Table 1 lists some typical values of normalized rms emittance and ion temperature measured in both SITEX and VITEX modes. For each beam condition, both transverse and parallel emittances were measured. The ion temperature measured for the transverse direction cannot be used to indicate the real ion temperature inside the

Table 1. Summary of typical ion temperature and emittance data

	SITEX		VITEX	
	Transverse measurement[a]	Parallel measurement[a]	Transverse measurement[b]	Parallel measurement[b]
Source slit dimensions $x \times y$, cm^2	0.21 × 0.16	0.21 × 0.16	0.1 × 2.0	0.1 × 2.0
Normalized rms emittance, π·cm·mrad	0.010 ± 0.005	0.003 ± 0.001	0.013	0.017
Ion temperature at extraction, eV	21	9.4	185	0.6
Current density, mA/cm^2	36	36	60	60

[a]Beamlet emittance in this direction.

[b]Entire beam emittance in this direction.

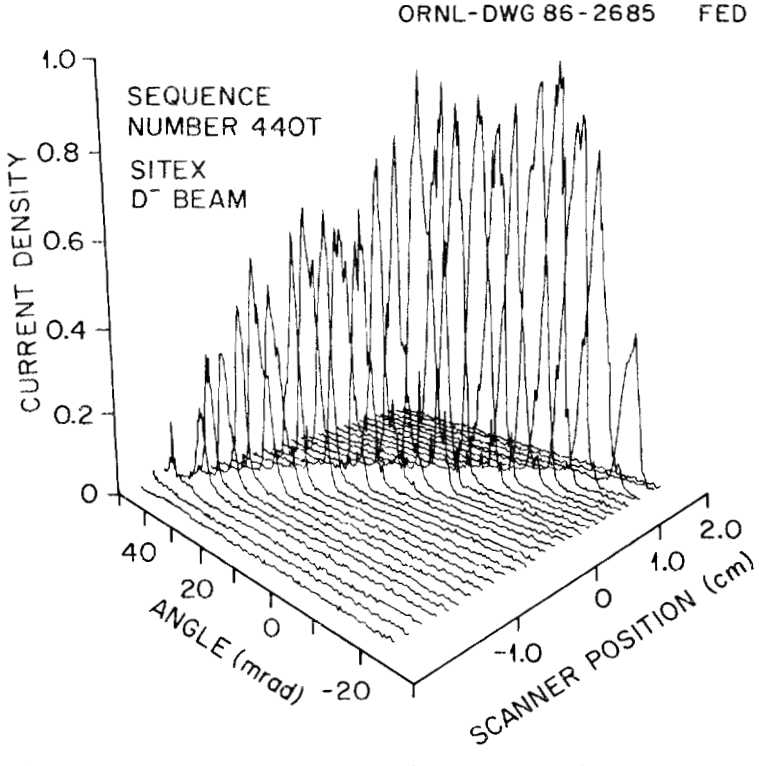

Fig. 11. Phase-space current density distribution for SITEX transverse measurement.

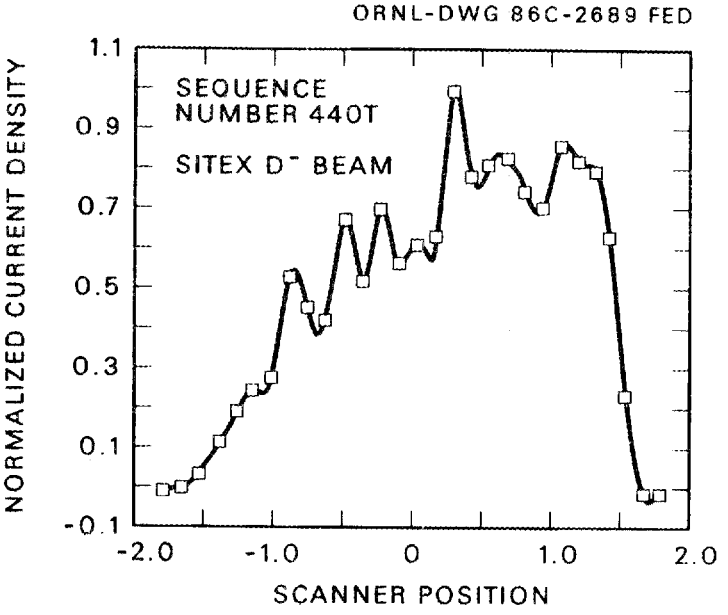

Fig. 12. Beam profile for SITEX transverse measurement.

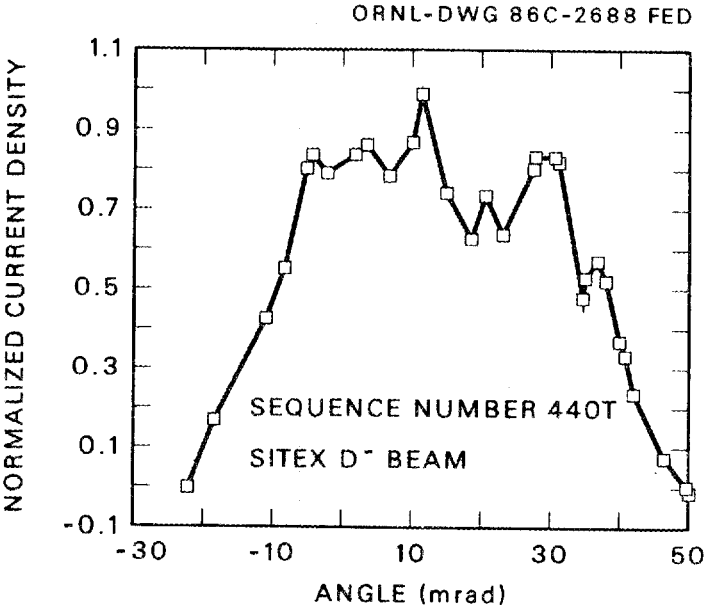

Fig. 13. Angular distribution for SITEX transverse measurement.

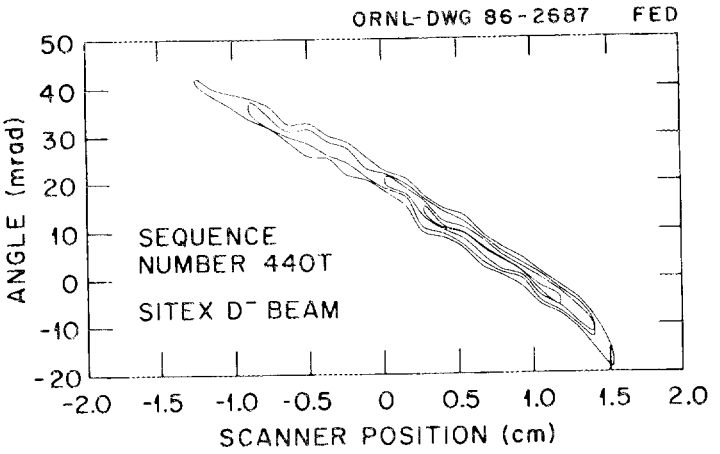

Fig. 14. Phase-space emittance diagram for SITEX transverse measurement.

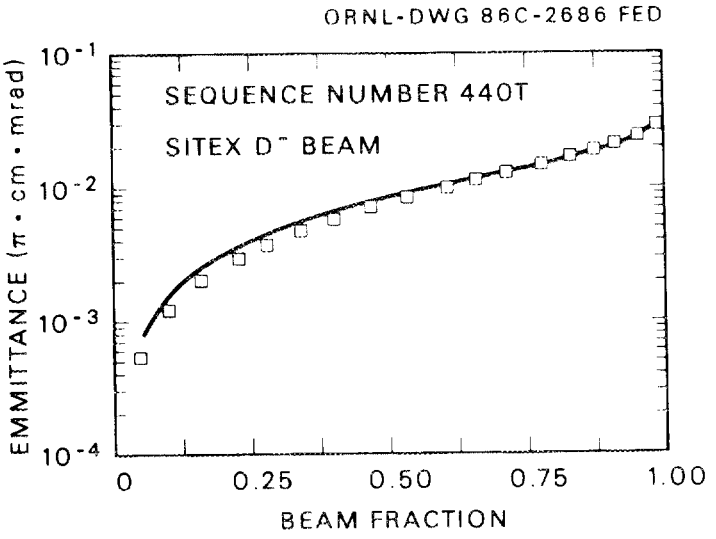

Fig. 15. Curve of rms emittance vs beam fraction for SITEX transverse measurement.

source, because the measured value is amplified substantially by the optics of the ion accelerator.

The accelerator structure was designed to provide optimum optics for ions created on a curved surface, as in the SITEX mode, and focused onto the extraction aperture. Hence, the transverse temperature for SITEX ions is raised by spatial compression in this direction, as well as by optical effects in the accelerator. This accelerator was not designed for volume-produced ion extraction, and hence the transverse optics are poor in the VITEX mode of operation. The temperatures measured parallel to the magnetic field are indicative of the actual temperatures with which the ions are formed and are not influenced by transverse compression or accelerator optics. The ion temperature of the beams formed by the VITEX source is well below 1 eV and is about ten times smaller than that for the SITEX source.

The current density for the ion beams analyzed in the SITEX mode (given in Table 1) is about 36 mA/cm^2. The highest current density for the SITEX source is about 50 mA/cm^2. For the VITEX H^- beams in Table 1, the current density is about 60 mA/cm^2. Optimization studies for increasing the beam current density are under way; the highest current density achieved is above 150 mA/cm^2.

5. DISCUSSION OF ERRORS

Of the several sources of error in these measurements, the following were the most important:

1. ripple in the high-voltage power supply,
2. variations in beam current,
3. scanner pickup noise, and
4. fluctuations in the magnetic field.

Errors 2 and 3 affected both the parallel and transverse measurements, whereas errors 1 and 4 were much more significant for transverse measurements. Large (1%) fluctuations in the magnetic field produced noticeable shifts in the distribution, and data taken under such conditions (which, fortunately, were rare) were discarded. Some of the noise in the scanner current pulses will eventually be eliminated by improvements in the electronics. With the present computer code, errors 1 and 2 can be minimized by using a shorter sampling time. However, the associated optics effect of changes in the perveance increases the difficulty of minimizing these two errors.

Fluctuations in the high voltage and in the magnetic field produce the same effect on the scanner current pulse for the transverse measurements. A change in either will shift the beam slightly relative to the scanner, and the angle at which the ions enter the scanner will change. For a shift ΔB in the magnetic field or $\Delta\phi$ in the high voltage, the beam shifts approximately a distance

$$\Delta R/R = \Delta B/B \quad \text{or} \quad \Delta R/R = \frac{1}{2}\Delta\phi/\phi \quad ,$$

where R is the average radius of the path followed by the ions. The shift in angle is approximately

$$\alpha \simeq \Delta R/R$$

and is more significant than the shift in position. A shift of 1% in the magnetic field strength produced the bend in the emittance diagram illustrated in Fig. 16.

This was an unusual case; the magnetic field seldom varied by more than a few tenths of a percent during the sequence of measurements. Variations in high voltage of 0.5% were common and could lead to shifts in the scanner of 2–3 mrad. Such shifts produce minor changes in the emittance vs beam fraction measurements but will have a significant effect on the rms emittance. Ion temperatures computed by these two methods should not be significantly changed by such excursions, but some care is required in determining the ion temperature from the angular distribution.

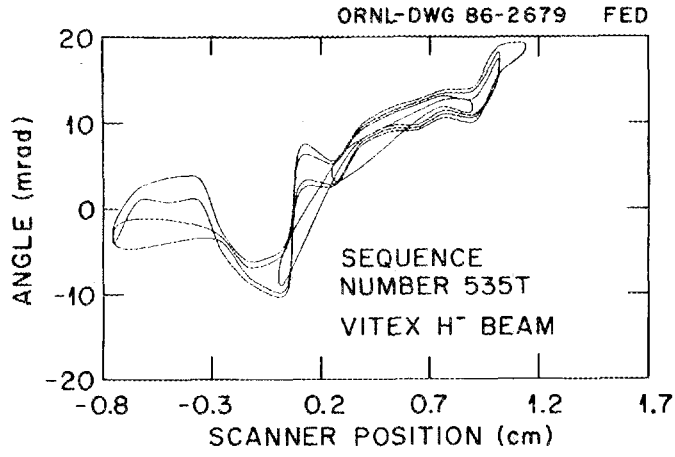

Fig. 16. Distorted phase-space emittance diagram.

These four sources of errors are present even if the scanner is not located in the magnetic field. Since we had to place the scanner in the field, we made further tests to determine whether the field had any effect. The associated errors are briefly mentioned below.

Another source of error for the parallel emittance scanner arose from the fact that one of the parallel plates was grounded while the other was swept with a deflecting voltage, causing the particle's energy to be changed at the entrance and exit of the analyzer. This effect was studied with the ORNL ion optics code[9] and was found to be minor. The slope of the linear portion of the θ vs V curve was only 0.53% less than the analytic value used in the code, leading to about a 1% error in the ion temperature.

In the perpendicular emittance scanner, the equations of motion are unsymmetric with respect to the particle entrance angle θ. While the parallel emittance scanner accepts incident angles of up to ± 125 mrad, the perpendicular scanner can only pass particles with incident angles between $+50$ and -110 mrad. While the θ vs V relationship is linear over the small θ sweeps used in the experiments, the slope is 4.5% greater than the analytic value, leading to a 4.5% error in the transverse emittance measurement.

The major error arising from having the scanner in the magnetic field is the spreading of the beam that occurs during its passage through the scanner. The force on an ion in the x-direction (perpendicular to the magnetic field) is

$$F_x = -e[E_s + E(t) - \dot{z}B] \quad ,$$

where E_s is the static field, $E(t)$ the ramp field, $\dot{z}$ the longitudinal speed of the ion, and B the magnetic field strength. For the transverse measurements, the static field is set to cancel the magnetic force for ions moving at a speed

$$\dot{z}_0 = E_s/B = BeR/M \quad .$$

For $\dot{z} = \dot{z}_0 + \Delta\dot{z}$, the residual magnetic force in the x-direction is

$$F_x = e\Delta\dot{z}B \quad .$$

The deflection Δx produced by this force as the ion traverses the scanner is approximately

$$\Delta x = \frac{1}{2}(F_x/M)t^2 = \frac{1}{2}(e\Delta\dot{z}B/M)(D/\dot{z}_0)^2 \quad ,$$

where D is the distance between scanner slits. For $\Delta\phi/\phi = 0.01$, $\Delta\dot{z} = 5000$ m/s. The other values inserted into this equation for a D^- beam case are as follows:

$$e = 1.6 \times 10^{-19} \text{ C} \quad ,$$

$$M = 3.34 \times 10^{-27} \text{ kg} \quad ,$$

$$B = 10^3 \text{ G} = 0.1 \text{ T} \quad ,$$

$$D = 4.128 \text{ cm} \quad ,$$

$$\dot{z}_0 = 9.8 \times 10^5 \text{ m/s} \quad .$$

The deflection Δx produced by variations in ϕ is about 0.002 cm. The scanner slit width for the SITEX measurements was 0.005 cm, so the spreading caused by the magnetic field effectively degrades the angular resolution by about 20% for the transverse measurements only. The measured transverse emittance could be 30% too high.

ACKNOWLEDGMENTS

The authors wish to thank the following people for their help on this project: D. E. Schechter for making the scanner work; S. C. Forrester for keeping the ion source running; B. E. Argo, G. C. Barber, D. O. Sparks, and R. E. Wright for their work on the electronics and power supplies; J. M. Friend and D. R. Overbey for their work on the computer hardware and software; D. H. Thompson for solving some of the electronics problems; and H. H. Haselton and J. H. Whealton for helpful discussions on data and error analysis.

REFERENCES

1. W. L. Stirling et al., "Normalized Emittance of the SITEX Negative Ion Source," *AIP Conf. Proc.* **111** (1983).

2. P. Allison et al., *An Emittance Scanner for Intense Low-Energy Beams*, Report LA-UR-83-707, Los Alamos National Laboratory, 1983.

3. C. Lejeune and J. Aubert, *Adv. Electron. Electron Phys.* **13A**, 159 (1980).

4. J. D. Lawson, *Physics of Charged Particle Beams*, Oxford University Press, 1977.

5. H. V. Smith, Jr., and P. Allison, "H^- Beam Emittance Measurements for the Penning and Magnetron Surface Plasma Sources," Los Alamos National Laboratory, unpublished data, 1985.

6. P. Allison "Emittance and Brightness in the White Horse Program," Los Alamos National Laboratory, unpublished data, AT-2:84–98 (1884).

7. P. Allison et al., Comparison of Measured Emittance of an H^- Ion Beam with a Simple Theory, LA-8808-MS, Los Alamos National Laboratory, 1984.

8. P. Allison, personal communication.

9. J. H. Whealton, *Nucl. Instrum. Methods* **189**, 55 (1981).

ORNL/TM-10186
Dist. Category UC-20a,d,f

INTERNAL DISTRIBUTION

1. M. A. Akerman
2. F. W. Baity
3. G. C. Barber
4. D. E. Bartine
5. L. A. Berry
6. W. R. Becraft
7–11. W. K. Dagenhart
12. R. A. Dory
13. R. H. Fowler
14. W. L. Gardner
15. J. T. Greer
16. H. H. Haselton
17. K. L. Kannan
18. M. M. Menon
19. O. B. Morgan
20. M. W. Rosenthal
21–25. P. M. Ryan
26. D. E. Schechter
27–31. W. L. Stirling
32. D. W. Swain
33–37. C. C. Tsai
38. J. H. Whealton
39. R. E. Wright
40. J. Sheffield
41–42. Laboratory Records Department
43. Laboratory Records, ORNL-RC
44. Central Research Library
45. Document Reference Section
46. Fusion Energy Division Library
47. Fusion Energy Division Publications Office
48. ORNL Patent Office

EXTERNAL DISTRIBUTION

49–53. J. J. Donaghy, Washington and Lee University, Lexington, VA 24450

54. Office of the Assistant Manager for Energy Research and Development, U.S. Department of Energy, Oak Ridge Operations Office, P. O. Box E, Oak Ridge, TN 37831

55. J. D. Callen, Department of Nuclear Engineering, University of Wisconsin, Madison, WI 53706-1687

56. J. F. Clarke, Director, Office of Fusion Energy, Office of Energy Research, ER-50 Germantown, U.S. Department of Energy, Washington, DC 20545

57. R. W. Conn, Department of Chemical, Nuclear, and Thermal Engineering, University of California, Los Angeles, CA 90024

58. S. O. Dean, Fusion Power Associates, Inc., 2 Professional Drive, Suite 249, Gaithersburg, MD 20760

59. H. K. Forsen, Bechtel Group, Inc., Research Engineering, P. O. Box 3965, San Francisco, CA 94105

60. J. R. Gilleland, L-644, Lawrence Livermore National Laboratory, P.O. Box 5511, Livermore, CA 94550

61. R. W. Gould, Department of Applied Physics, California Institute of Technology, Pasadena, CA 91125
62. R. A. Gross, Plasma Research Laboratory, Columbia University, New York, NY 10027
63. D. M. Meade, Princeton Plasma Physics Laboratory, P.O. Box 451, Princeton, NJ 08544
64. M. Roberts, International Programs, Office of Fusion Energy, Office of Energy Research, ER-52 Germantown, U.S. Department of Energy, Washington, DC 20545
65. W. M. Stacey, School of Nuclear Engineering and Health Physics, Georgia Institute of Technology, Atlanta, GA 30332
66. D. Steiner, Nuclear Engineering Department, NES Building, Tibbetts Avenue, Rensselaer Polytechnic Institute, Troy, NY 12181
67. R. Varma, Physical Research Laboratory, Navrangpura, Ahmedabad 380009, India
68. Bibliothek, Max-Planck Institut fur Plasmaphysik, Boltzmannstrasse 2, D-8046 Garching, Federal Republic of Germany
69. Bibliothek, Institut für Plasmaphysik, KFA Jülich GmbH, Postfach 1913, D-5170 Jülich, Federal Republic of Germany
70. Bibliothek, KfK Karlsruhe GmbH, Postfach 3640, D-7500 Karlsruhe 1, Federal Republic of Germany
71. Bibliotheque, Centre de Récherches en Physique des Plasmas, Ecole Polytechnique Federale de Lausanne, 21 Avenue des Bains, CH-1007 Lausanne, Switzerland
72. F. Prevot, CEN/Cadarache, Departement de Recherches sur la Fusion Contrôlée, F-13108 Saint-Paul-lez-Durance Cedex, France
73. Bibliothèque, CEN/Cadarache, F-13108 Saint-Paul-lez-Durance Cedex, France
74. Library, Culham Laboratory, UKAEA, Abingdon, Oxfordshire, OX14 3DB, England
75. Library, JET Joint Undertaking, Abingdon, Oxfordshire OX14 3EA, England
76. Library, FOM-Instituut voor Plasmafysica, Rijnhuizen, Edisonbaan 14, 3439 MN Nieuwegein, The Netherlands
77. Library, Institute of Plasma Physics, Nagoya University, Chikusa-ku, Nagoya 464, Japan
78. Library, International Centre for Theoretical Physics, P.O. Box 586, I-34100 Trieste, Italy
79. Library, Centro Richerche Energia Frascati, C.P. 65, I-00044 Frascati, Rome, Italy
80. Library, Plasma Physics Laboratory, Kyoto University, Gokasho, Uji, Kyoto, Japan

81. Plasma Research Laboratory, Australian National University, P.O. Box 4, Canberra, A.C.T. 2000, Australia
82. Library, Japan Atomic Energy Research Institute, Naka-machi, Naka-gun, Ibaraki-ken 311-02, Japan
83. Library, Japan Atomic Energy Research Institute, Tokai, Ibaraki-ken 319-11, Japan
84. T. V. George, Plasma Technologies Branch, Division of Development and Technology, Office of Fusion Energy, Office of Energy Research, ER-531 Germantown, U.S. Department of Energy, Washington, DC 20545
85. G. M. Haas, Fusion Technologies Branch, Division of Development and Technology, Office of Fusion Energy, Office of Energy Research, ER-533 Germantown, U.S. Department of Energy, Washington, DC 20545
86. E. Oktay, Division of Confinement Systems, Office of Fusion Energy, Office of Energy Research, ER-55 Germantown, U.S. Department of Energy, Washington, DC 20545
87. H. S. Staten, Plasma Technologies Branch, Division of Development and Technology, Office of Fusion Energy, Office of Energy Research, ER-531 Germantown, U.S. Department of Energy, Washington, DC 20545
88. R. L. Abbott, U.S. Army, SCD, DASD-H-D, P.O. Box 1500, Huntsville, AL 35807
89. P. Allison, AT-2, MS-H818, Los Alamos National Laboratory, P.O. Box 1663, Los Alamos, NM 87545
90. D. S. Beard, Division of Development and Technology, Office of Fusion Energy, Office of Energy Research, ER-531 Germantown, U.S. Department of Energy, Washington, DC 20545
91. P. Caruso, U.S. Army, SDC, DASD-H-D, P.O. Box 1500, Huntsville, AL 35807
92. W. S. Cooper, Bldg. 4, Lawrence Berkeley Laboratory, University of California, Berkeley, CA 94088
93. R. J. Dowling, Division of Development and Technology, Office of Fusion Energy, Office of Energy Research, ER-531 Germantown, U.S. Department of Energy, Washington, DC 20545
94. G. R. Edlin, U.S. Army, SDC, DASD-H-D, P.O. Box 1500, Huntsville, AL 35807
95. G. H. Gillespie, Physical Dynamics, Inc., 4350 Executive Drive, Suite 135, San Diego, CA 92121
96. L. R. Grisham, Princeton Plasma Physics Laboratory, P.O. Box 451, Princeton, NJ 08544
97. M. C. Hawie, U.S. Army, SDC, DASD-H-D, P.O. Box 1500, Huntsville, AL 35807
98. J. Kim, Rm. 34/27, GA Technologies, Inc., P.O. Box 85608, San Diego, CA 92138

99. M. Lavan, U.S. Army, SDC, DASD-H-D, P.O. Box 1500, Huntsville, AL 35807
100. T. G. Miller, General Research Corporation, 307 Wynn Dr., Huntsville, AL 35805
101. T. Roberts, U.S. Army, SDC, DASD-H-D, P.O. Box 1500, Huntsville, AL 35807
102. R. R. Stevens, Jr., AT-2, MS-H818, Los Alamos National Laboratory, P.O. Box 1663, Los Alamos, NM 87545
103. L. Stewart, Rm. 13/264, GA Technologies, Inc., P.O. Box 85608, San Diego, CA 92138
104. B. Strickland, U.S. Army, SDC, DASD-H-D, P.O. Box 1500, Huntsville, AL 35807

105–248. Given distribution as shown in TIC-4500, Magnetic Fusion Energy (Category UC-20a,d,f: Plasma Systems, Fusion Systems, Experimental Plasma Physics)